Available online at www.sciencedirect.com
SCIENCE DIRECT
Cement and Concrete Research 36 (2006) 749 – 760
Cement and Concrete Research

Non-structural cracking in RC walls Part I. Finite element formulation

Hyo-Gyoung Kwak *, Soo-Jun Ha, Jin-Keun Kim

Department of Civil and Environmental Engineering, Korea Advanced Institute of Science and Technology, Daejeon 305-701, South Korea

Received 17 October 2005; accepted 6 December 2005

Abstract

In this paper, a three-dimensional finite element model for the analysis of non-structural cracks occurring in reinforced concrete (RC) walls is introduced. The numerical model could take into account both time-dependent temperature variations due to hydration heat and non-uniform moisture distribution during drying, and the coupling effect between the heat transfer and the moisture diffusion. Calculation of the temperature and internal relative humidity variations of RC walls is followed by determination of stresses due to thermal gradients, differential drying shrinkage, and average drying shrinkage. The mechanical properties of early age concrete, determined from numerous experimental studies, are taken into consideration to improve the accuracy of the numerical results, and a discrete steel element derived using the equivalent nodal force concept is also used to simulate reinforcing steels embedded in a concrete matrix. The validity of the proposed procedure is verified by comparing the measured experimental data with the analytical results for RC walls.

Keywords: Hydration; Shrinkage; Temperature; Humidity; Finite element analysis

1. Introduction

Cracks in concrete structures can generally be classified into two classes, structural cracks and non-structural cracks. These cracks can indicate major structural problems and/or mar the appearance of a monolithic construction, and they can prematurely expose reinforcing steel to oxygen and moisture and make the steel more susceptible to corrosion. While the specific causes of cracking are manifold, cracks are normally caused by stresses that develop in concrete due to the restraint of volumetric change or to loads applied to the structure. Unlike structural cracks caused by external loads, non-structural cracks result from a variety of causes related to the material properties of concrete and construction practices, while a number of factors concurrently contribute to the occurrence of non-structural cracks. The dominant causes of cracks in concrete structures also depend on the type of structure, as well as the nature of the cracking itself.

Plastic shrinkage cracking in concrete occurs most commonly on the exposed surfaces of freshly placed floors and slabs that have large surface areas, while wall structures usually suffer from uniformly distributed transverse cracks occurring in hardened concrete due to drying shrinkage and hydration heat. Since the objective of this paper is to develop a three-dimensional finite element program for the analysis of cracks in reinforced concrete (RC) walls, the influence of hydration heat and differential drying shrinkage is emphasized.

Drying shrinkage is caused by a loss of moisture from the cement paste constituent. The moisture content decreases due to moisture diffusion after the concrete is exposed to ambient air and the loss of moisture causes the volume of the paste to contract. This, in turn, leads to shrinkage stress and shrinkage cracking when the tensile strength of concrete is exceeded. The magnitude of the tensile stresses is influenced by a combination of factors, including the amount of shrinkage, the degree of restraint, the modulus of elasticity, the amount of creep, etc. [1]. Moreover, temperature differences within a concrete structure may occur as a result of cement hydration, and these temperature differences result in differential volume changes. When the tensile strains due to the differential volume changes

* Corresponding author. Tel.: +82 42 869 3621; fax: +82 42 869 3610.
E-mail address: khg@kaist.ac.kr (H.-G. Kwak).

0008-8846/$ - see front matter © 2005 Elsevier Ltd. All rights reserved.
doi:10.1016/j.cemconres.2005.12.001

exceed their tensile strain capacity, concrete will crack. Cracks in concrete have many causes, and each cause needs to be analyzed for successful crack control of a concrete structure.

To estimate the contribution of each influencing factor to the cracking, many experimental and numerical studies have been conducted [2–10]. Many experimental studies to verify the material properties related to hydration heat and drying shrinkage were performed [11–15], and the introduction of accurate and general theoretical models to describe the material properties was the main research objective [2,4,16–18]. Recently, many advanced analytical and/or numerical approaches have also been performed to simulate the cracking behavior of concrete [3,6–8,10,19], owing to the numerous material models related to non-structural cracks of concrete [2,4,9,16,18,20].

In spite of these extensive numerical approaches, several problems remain in predicting the non-structural cracking behavior of RC walls, because most of the numerical approaches [3,6–8,19] focus on a representative cause such as hydration heat or drying shrinkage, while in actuality numerous influencing factors contribute concurrently to the occurrence of cracks. Moreover, many influencing factors are also ignored or assumed as simple constant values without any verification based on experimental studies.

In this paper, an improved numerical approach for the analysis of non-structural cracks occurring in RC walls is introduced. Unlike previous numerical approaches, both time-dependent temperature variation due to hydration heat and moisture diffusion during drying are taken into account. In advance, material models describing the material properties of concrete at an early age [4,9,20] are used to improve the accuracy of the numerical results, and a discrete steel element derived using the equivalent nodal force concept [21] is also used to simulate reinforcing steels embedded in a concrete matrix. Finally, the reliability of the proposed numerical approach is verified by comparing the calculated prediction results with the measured experimental data for RC walls.

2. Heat transfer analysis

2.1. Thermal properties of concrete

Concrete is a heterogeneous material, the components of which have different thermal properties. As such, the thermal properties of concrete are affected by various factors, including types of material used and volume ratios of aggregate, concrete temperature, water content, porosity, etc. [1].

Since the thermal conductivity of concrete is one of the key parameters needed to predict temperature variation during hydration, the reliability of the proposed numerical approach depends on the accuracy of the thermal conductivity of concrete, especially at very early ages. The coefficient of thermal conductivity of concrete is influenced by the density of concrete, the type of aggregates used and the moisture content of concrete [1]. A typical value of the thermal conductivity of concrete is in the range of 2.50–2.92 W/m °C according to JCI [17], and in the range of 1.98–2.94 W/m °C according to ACI [12]. To describe the thermal conductivity of early age concrete, the following regression equation obtained from many experimental tests for early age concrete [9] is adopted in this study.

$$k_c = k_o(0.34 + 1.03\mathrm{AG})(0.8 + 0.2R_h)(1.04 - 0.002T) \quad (1)$$

where AG=aggregate volume fraction in concrete, R_h=relative humidity, T=temperature (°C), and k_o is the reference thermal conductivity of concrete when AG=0.64 and T=20 °C.

The specific heat is the amount of heat required per unit mass to change a unit temperature over a small range of temperature. The specific heat of normal weight concrete varies only slightly with the type of aggregate used as most of the rocks have similar mineralogical content. However, the specific heat of cement paste varies strongly depending on its porosity, water content, and specimen temperature characteristics. Therefore, the variation of specific heat of concrete depends on these factors as well [1]. A representative specific heat value of concrete is in the range of 1130–1300 J/kg °C according to JCI [17], and 920–1000 J/kg °C according to ACI [12].

The degree of heat exchange by atmospheric convection is determined by a coefficient of atmosphere convection representing any relation with the wind velocity. It was reported that the coefficient of atmosphere convection is in the range of 14–15 W/m^2 °C [17], and 9–13 W/m^2 °C [15] when the wind velocity ranges from 2 to 3 m/s. Ohzawa [17] proposed the coefficient of atmosphere convection, h_a, as a function of wind velocity as h_a=11.2+1.30v, where v is the wind velocity (m/s). In spite of this consideration for wind velocity, the direct application of this equation still has a limitation in considering the variation according to the formworks used.

When the formwork is used on the surface of the concrete specimen, the difference in temperature between the interior and exterior surface of the specimen decreases, because the heat release rate to ambient air decreases due to the formwork, which acts as a barrier to heat loss. In advance, the heat release rate also depends on the material type and thickness of formwork used. To take into account the influence of the formwork, the following equations obtained from the experimental results for early age concrete [9] are adopted in this paper.

$$\begin{aligned} h_a &= 8.68 + 1.20v : \text{steel formwork} \\ h_a &= 6.89 + 1.66v : \text{wood formwork with thickness} = 1\ \text{cm} \\ h_a &= 4.30 + 0.41v : \text{wood formwork with thickness} = 2\ \text{cm} \end{aligned} \quad (2)$$

where v is the wind velocity (m/s).

2.2. Governing heat transfer equations

When a three-dimensional body is subjected to heat transfer conditions, it can be assumed that the material obeys Fourier's law of heat conduction [22];

$$q_i = -k_i \frac{\partial T}{\partial i}, \quad q_{i+\mathrm{d}i} = q_i + \frac{\partial q_i}{\partial i}\mathrm{d}i \quad (i = x, y, z) \quad (3)$$

where q_i is the heat flux per unit time and area, T is the temperature of the body, and k_i are the thermal conductivities corresponding to the principal axes x, y, and z. From the equilibrium condition of heat transfer including the internal hydration heat and the heat flux in Eq. (3), the equilibrium equation of heat transfer can be expressed by [22]

$$\frac{\partial}{\partial i}\left(k_i \frac{\partial T}{\partial i}\right) + q^{\mathrm{B}} = 0 \tag{4}$$

where q^{B} is the rate of internal heat generated per unit volume. Eq. (4) is for a steady-state heat analysis where no phase change and latent heat effects are assumed. However, the hydration process of concrete accompanies the temperature change of body; hence a transient heat analysis must be conducted, and the term q^{B} in Eq. (4) must be replaced by $q^{\mathrm{B}} - \rho c \mathrm{d}T/\mathrm{d}t$, where c is the specific heat and ρ is the density of concrete.

The equilibrium equation of heat transfer in Eq. (4) includes only heat transfer caused by internal hydration heat and thermal conductivity. In order to consider boundary conditions on the surfaces of the body caused by atmosphere convection, the following condition representing the heat flux by atmosphere is introduced:

$$q^{\mathrm{a}} = k_{n,\mathrm{a}} \left.\frac{\partial T}{\partial n}\right|_{\Gamma_{\mathrm{sa}}} = h_{\mathrm{a}}\left(T_{\mathrm{a}} - T_{\mathrm{s,a}}\right) \tag{5}$$

where $k_{n,\mathrm{a}}$ are the coefficients of thermal conductivity for the atmosphere in n direction, where subscript n represents the normal direction to the convection area. Γ_{sa} and h_{a} are the boundary surfaces and the coefficients of heat convection for atmosphere, respectively. T_{a} and $T_{\mathrm{s,a}}$ are the temperatures of atmosphere and the concrete temperatures on the convection boundary surface of atmosphere, respectively.

2.3. Finite element formulation

Heat transfer and concrete stresses can be determined using the finite element method employing eight-node isoparametric solid elements. Since the temperature $T(x, y, z, t)$ is spread over an element by $T(x, y, z, t) = [N(x, y, z)]\{T(t)\}$, where $N(x, y, z)$ is a matrix containing the shape functions and $T(t)$ is the nodal temperature vector at time t, Eq. (4) can be written in the following matrix form by applying the Galerkin weighted residual method [22]:

$$[C]_{\mathrm{T}}\{\dot{T}\} + [K]_{\mathrm{T}}\{T\} = \{Q\}_{\mathrm{T}} \tag{6}$$

where $[C]_{\mathrm{T}} = \sum_{\mathrm{e}}[C^{\mathrm{con}}] = \sum_{\mathrm{e}} \int_V \rho c [N]^{\mathrm{T}}[N]\mathrm{d}V$ is the matrix for specific heat capacity, $[K]_{\mathrm{T}} = \sum_{\mathrm{e}}([K^{\mathrm{con}}] + [K^{\mathrm{air}}]) = \sum_{\mathrm{e}} (\int_V k[B]^{\mathrm{T}}[B]dV + \int_S h_{\mathrm{a}}[N]^{\mathrm{T}}[N]\mathrm{d}S)$ is the matrix for thermal conductivity, and $\{Q\}_{\mathrm{T}} = \sum_{\mathrm{e}}(\{Q^{\mathrm{hyd}}\} + \{Q^{\mathrm{air}}\}) = \sum_{\mathrm{e}}(\int_V q^{\mathrm{B}} [N]^{\mathrm{T}}\,\mathrm{d}V + \int_S h_{\mathrm{a}} T_{\mathrm{a}} [N]^{\mathrm{T}}\mathrm{d}S)$ is the total heat flux vector for internal hydration heat $\{Q^{\mathrm{hyd}}\}$ and heat convection of atmosphere $\{Q^{\mathrm{air}}\}$. $[B]$ is the matrix for the derivative of the shape function with respect to natural coordinates. c is the coefficient of specific heat for concrete, and ρ is the density of concrete. k is the coefficient of thermal conductivity for concrete, and h_{a} is the coefficient of heat convection for atmosphere.

3. Moisture diffusion analysis

If concrete is exposed to ambient air at early ages, water movement takes place due to surface evaporation and moisture diffusion, and a non-uniform cross-sectional moisture distribution, which in turn causes differential drying shrinkage. From this type of differential drying shrinkage, tensile stress occurs on the exposed surface of concrete structures and may result in crack formation. If external restraints to the volume change are added, a remarkable increase in the potential for cracking occurs. Therefore, to estimate the differential drying shrinkage and its effect on cracking, an accurate and general theoretical model is required.

3.1. Governing moisture diffusion equations

The moisture flux J is proportional to the gradient of the pore relative humidity, and can be expressed by $J = -k\mathrm{grad}h$, where h is the pore relative humidity and k is the permeability. The specific water content w is a function of pore relative humidity h in the desorption isotherm, i.e., $w = w(h)$, so that the mass balance equation can be expressed as follows [19]:

$$\frac{\partial w}{\partial t} = \frac{\partial w}{\partial h}\frac{\partial h}{\partial t} = \frac{1}{c}\frac{\partial h}{\partial t} = -\mathrm{div}J \tag{7}$$

where $\partial w/\partial h$ is the moisture capacity, which represents the slope of the desorption isotherm. Accordingly, the nonlinear moisture diffusion equation can be represented by the expression

$$\frac{\partial h}{\partial t} = c\ \mathrm{div}(k\ \mathrm{grad}\ h) = \mathrm{div}(D\ \mathrm{grad}\ h) \tag{8}$$

where D is the moisture diffusion coefficient, and is defined as $c{\cdot}k$. The moisture diffusion coefficient is dependent on the relative humidity and temperature. On the basis of many experimental studies for early age concrete, Mihashi and Numao [4] proposed the moisture diffusion coefficient is expressed as a function of the pore relative humidity and temperature

$$D(h, T) = D_1 f_1(h) f_2(T) f_3(T) \tag{9}$$

where

$$f_1(h) = \left(\alpha + \frac{1-\alpha}{1 + [(1-h)/(1-h_{\mathrm{c}})]^n}\right) \tag{10}$$

$$f_2(T) = \left(\frac{T}{T_0}\right)^{N_1} \exp\left\{\frac{U}{R}\left(\frac{1}{T_0} - \frac{1}{T}\right)\right\} \tag{11}$$

$$f_3(T) = \exp\left\{\left(\frac{T-273}{90}\right)^{N_2}\right\} \tag{12}$$

D_1 is the maximum of $D(h, T)$ for $h=1.0$ and the reference temperature $T_0=293$ K, T is the absolute temperature. U is the activation energy of low temperature moisture diffusion, and R is the gas constant. α, h_c, n, N_1, and N_2 are the material parameters depending on the concrete mixture and curing conditions.

For the boundary condition of moisture, it is necessary to correlate the surface moisture with the humidity of the environmental atmosphere. On the exposed surface S, the boundary condition is as follows.

$$D\left(\frac{\partial h}{\partial n}\right)_S = f(h_{en} - h_s) \tag{13}$$

where f is the surface factor (m/h) determined through a regression of the experimental data [16]. Usually this factor can be expressed as a function of the water/cement ratio [16], and the relation of $f=2.17\times10^{-3}$ (w/c)-8.56×10^{-4} is used in this paper. h_{en} is the environmental humidity, and h_s is the relative humidity on the exposed surface. Bazant and Najjar dealt with this problem by assuming an additional thickness to the specimen, i.e., the equivalent surface thickness [13]. Comparing analytical results with experimental ones, Bazant reported that the value of the equivalent surface thickness is 0.75 mm.

3.2. Finite element formulation

The relative humidity $H(x, y, z, t)$ in an element can also be expressed in terms of the relative humidity $h(t)$ at each node by $H(x, y, z, t)=[N(x, y, z)]\{h(t)\}$. From the same derivation procedure to that used in the case of heat transfer, the differential governing equation of Eq. (8) can be represented by the following matrix form.

$$[C]_H\{\dot{H}\} + [K]_H\{H\} = \{Q\}_H \tag{14}$$

where $[C]_H = \sum_e[C^{con}] = \sum_e \int_V [N]^T[N]dV$ is the moisture capacity matrix, $[K]_H = \sum_e([K^{con}] + [K^{air}]) = \sum_e(\int_V D[B]^T[B]dV + \int_S f[N]^T[N]dS)$ is the moisture diffusivity stiffness matrix, and $\{Q\}_H = \sum_e\{Q^{air}\} = \sum_e \int_S fh_{en}[N]^T dS$ is the moisture load vector.

4. Construction of equilibrium equation

The solutions for the heat transfer and moisture diffusion equations can be obtained by integrating Eqs. (6) and (14) using a numerical step-by-step procedure at any time t, and direct integration methods are generally used. In this paper, the Crank-Nicolson method, which is unconditionally stable for selection of the time step Δt, is used [22]. In particular, there is no difference in the solution procedure even if there are different solutions for both equations, and thus the same direct integration method is used. On the other hand, many experimental studies [1,2,4,9] have noted that the thermal conductivity k and the moisture diffusion coefficient D depend on both temperature and relative humidity. This means that Eqs. (6) and (14) are coupled, and the calculation of exact values for both coefficients requires an iterative solution procedure at each time step.

Nevertheless, a piece-wise linear analysis with relatively small time intervals seems to be more effective than a rigorous nonlinear iterative analysis, because the temperature and the relative humidity in an early age concrete are still maintained within the range of minor influence on the thermal conductivity and the moisture diffusion coefficient, respectively [4,9]. At an arbitrary time step t_n, the temperature and moisture distributions in an elastic body can be found by solving the governing equations of (6) and (14), and the same procedures are repeated at the next time step t_{n+1} after revising the material properties on the basis of the results obtained at the previous time step t_n. Only the material properties that can consider the coupling effect by the heat transfer and the moisture diffusion are used in defining the governing equations of (6) and (14). These values were determined from numerous experimental studies [2,4,9,19], and more details, from an introduction of a regression curve to correlation studies between experimental data and analytical results, can be found elsewhere [4,9,19].

Ultimately, the numerical results obtained in this study are expected to be slightly different from those obtained by previous numerical studies [3,6,7,19], because, while each phenomenon for the heat transfer or the moisture diffusion was

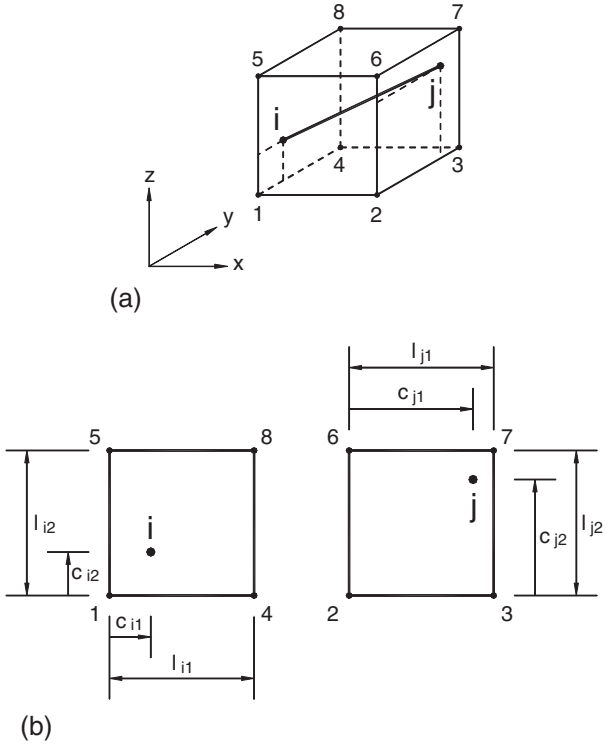

Fig. 1. Steel element embedded in concrete element. (a) A reinforced concrete element, (b) two end plans crossed by a reinforcing steel.

carefully addressed, the coupling effect was not taken into account in previous studies.

When the temperature increments ΔT and moisture increments Δh at an arbitrary time t_n are determined with the temperature and moisture calculated from Eqs. (6) and (14), the internal deformations and stresses in an elastic body can be obtained by solving the following equilibrium equation constructed on the basis of the least work principle [22].

$$[K]\{U\} = \{F\} \tag{15}$$

where $[K] = \sum_e [K_e] = \sum_{e_c} [K]_c + \sum_{e_s} [K_{GL}]_s = \sum_{e_c} (\int_V [B]^T [D][B] dV) + \sum_{e_s} [K_{GL}]_s$ is the global stiffness matrix, and $\{F\}$ is the nodal force vector. Based on the principle of superposition, total concrete strain $\varepsilon_c(t_n)$ at any time t_n is assumed to be composed of the mechanical strain $\varepsilon_c^m(t_n)$ caused by short-term service loads and the non-mechanical strain $\varepsilon_c^{nm}(t_n)$, which consists of temperature strain $\varepsilon_c^{th}(t_n)$, shrinkage strain $\varepsilon_c^{sh}(t_n)$, and creep strain $\varepsilon_c^{cr}(t_n)$. That is, $\varepsilon_c(t_n) = \varepsilon_c^m(t_n) + \varepsilon_c^{th}(t_n) + \varepsilon_c^{sh}(t_n) + \varepsilon_c^{cr}(t_n)$. Accordingly, the nodal force vector can be represented by the superposition of each force component caused by the non-mechanical strains.

$$\{F\} = \sum_{e_c} (\{f_T\}_c + \{f_S\} + \{f_C\}) + \sum_{e_s} \{f_T\}_s \tag{16}$$

where $\{f_T\}_c = \int_V [B]^T [D] \{\varepsilon_c^{th}\} dV$, $\{f_S\} = \int_V [B]^T [D] \{\varepsilon_c^{sh}\} dV$, $\{f_C\} = \int_V [B]^T [D] \{\varepsilon_c^{cr}\} dV$, $\varepsilon_c^{th} = \alpha \cdot \Delta T$ where α is termed the thermal dilation coefficient; $\varepsilon_c^{sh} = \varepsilon_{sh\infty} \cdot \{f_s(h_{n+1}) - f_s(h_n)\}$ and $f_s(h) = 0.97 - 1.895(h - 0.2)^3$, where $\varepsilon_{sh\infty}$ is the ultimate shrinkage coefficient given in the design code [18]; and the creep strain ε_c^{cr} is determined in accordance with the first-order algorithm based on the expansion of a degenerate kernel of compliance function [18,23]. $[B]$ is a strain matrix generally composed of derivatives of the shape functions, and the material matrix $[D]$ is updated at every time step to consider age-dependent properties of concrete by using the relation proposed by Kim et al. [20] on the basis of experimental studies for early age concrete. Moreover, thermal strain is the only non-mechanical strain expected for steel, and hence the nodal force

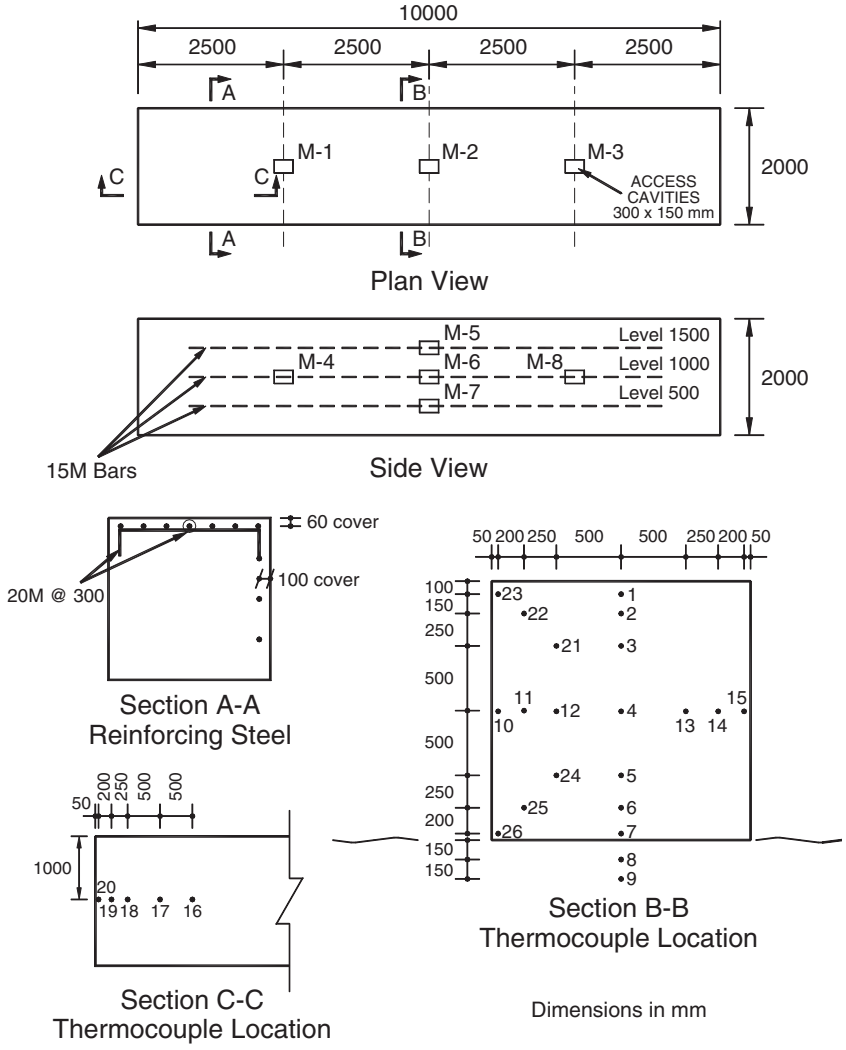

Fig. 2. Experimental specimen and instrumentation [7].

caused by the reinforcing steel $\{f_T\}_s$ can be determined on the basis of the temperature difference at both end points i and j in Fig. 1.

Since the stresses in the reinforcing steel are expected to be less than the yield stress, the reinforcing steel is modeled as a linear elastic material. In advance, an improved discrete reinforcing steel model is used in construction of an element stiffness matrix. In the proposed discrete model, the reinforcing steel is represented by a one-dimensional truss element, which is embedded in the concrete element as shown in Fig. 1. The nodes of the steel element do not need to coincide with the nodes of the concrete element. In this study the end displacements of the steel element are assumed to be compatible with the boundary displacements of the concrete element so that a perfect bond is implied.

Since the end points of the reinforcing bar element do not generally coincide with the nodes of the concrete element in Fig. 1, the one-dimensional truss element with constant strain has to undergo transformation before it can be assembled together with the concrete element stiffness matrix. This can be formally expressed by the following relation:

$$[K_{GL}]_s = [T_2]^T[T_1]^T[K_{LO}]_s[T_1][T_2] \tag{17}$$

where

$$[T_1] = \begin{bmatrix} \cos\theta_{xi} & \cos\theta_{yi} & \cos\theta_{zi} & 0 & 0 & 0 \\ 0 & 0 & 0 & \cos\theta_{xj} & \cos\theta_{yj} & \cos\theta_{zj} \end{bmatrix} \tag{18}$$

and θ is the angle between the axis of the reinforcing steel and the global axis of the structure.

A transformation matrix $[T_2]$ can be derived with the procedure used to establish the consistent nodal forces of the finite element method. Since an eight-node isoparametric solid element is used in the three-dimensional mesh representation of the member, the transformation matrix $[T_2]$ has the following form when the reinforcing bar element crosses the two planes of a concrete element; these planes are bounded by four nodes (1, 4, 8, and 5) at the steel end point i and four nodes (2, 3, 7, and 6) at the other end point j,

$$[T_2] = \begin{bmatrix} \mathbf{A}_{1i} & \mathbf{0} & \mathbf{0} & \mathbf{A}_{2i} & \mathbf{A}_{4i} & \mathbf{0} & \mathbf{0} & \mathbf{A}_{3i} \\ \mathbf{0} & \mathbf{A}_{1j} & \mathbf{A}_{2j} & \mathbf{0} & \mathbf{0} & \mathbf{A}_{4j} & \mathbf{A}_{3j} & \mathbf{0} \end{bmatrix} \tag{19}$$

where

$$\mathbf{A}_{1k} = \begin{bmatrix} (1-p_k)(1-q_k) & 0 & 0 \\ 0 & (1-p_k)(1-q_k) & 0 \\ 0 & 0 & (1-p_k)(1-q_k) \end{bmatrix}$$

$$\mathbf{A}_{2k} = \begin{bmatrix} p_k(1-q_k) & 0 & 0 \\ 0 & p_k(1-q_k) & 0 \\ 0 & 0 & p_k(1-q_k) \end{bmatrix}$$

$$\mathbf{A}_{3k} = \begin{bmatrix} p_kq_k & 0 & 0 \\ 0 & p_kq_k & 0 \\ 0 & 0 & p_kq_k \end{bmatrix}$$

$$\mathbf{A}_{4k} = \begin{bmatrix} (1-p_k)q_k & 0 & 0 \\ 0 & (1-p_k)q_k & 0 \\ 0 & 0 & (1-p_k)q_k \end{bmatrix} \tag{20}$$

$p_k = 2c_{k1}/l_{k1} - 1$, $q_k = 2c_{k2}/l_{k2} - 1$, k means i or j, and $\mathbf{0}$ is the 3×3 null matrix.

5. Numerical examples

To verify the efficiency of the numerical model which has been presented, three RC structures have been investigated. The first specimen is a large concrete block tested by Ayotte et al. [7]. This specimen was designed to observe the thermal behavior of a concrete block subjected first to heat of hydration development and subsequent freeze and thaw cycles. The specimen was built inside a large heated shelter in which the temperature was maintained at 30 to 32 °C during construction. The cross-section dimensions of the specimen and the reinforcement layout are represented in Fig. 2, and the material properties including composition of the concrete matrix are summarized in Table 1. Instrumentation of this specimen consisted of 26 T-type thermocouples and 8 pairs of mechanical strain targets (M-1–M-8) on the skin reinforcement. The exact locations for each instrument are presented in Fig. 2, and more details related to the experimental study can be found elsewhere [7].

Thermal analyses were made with the program ADINA-T [7], which is well suited for a transient analysis, by Ayotte et al. [7]. The finite element model used to simulate the thermal behavior of the specimen considered the heat generation and the surface conditions. Exposure to ambient air was modeled by defining convection boundary conditions. The dissipation of heat through the rock foundation was also considered by adding

Table 1
Material properties used in the analysis

Material property	Concrete	Rock
Water/cement ratio	0.5	–
Unit quantity of cement (kg/m^3)	310	–
28-day compressive strength (MPa)	27.5	–
Density (kg/m^3)	2370	2760
Specific heat (J/kg °C)	1005	670
Thermal conductivity (W/m °C) [20 °C, RH 100%]	2.00	2.60
Convection coefficient (W/m^2 °C)		
With formwork	4.80	–
Exposed	23.0	–
Maximum adiabatic temperature rise (°C)	31.0	–
Reaction rate (day^{-1})	1.038	–
Maximum moisture diffusion coefficient (m^2/h)	1.53×10^{-6}	1.53×10^{-6}
Surface factor (m/h) [20 °C]	1.81×10^{-5}	–

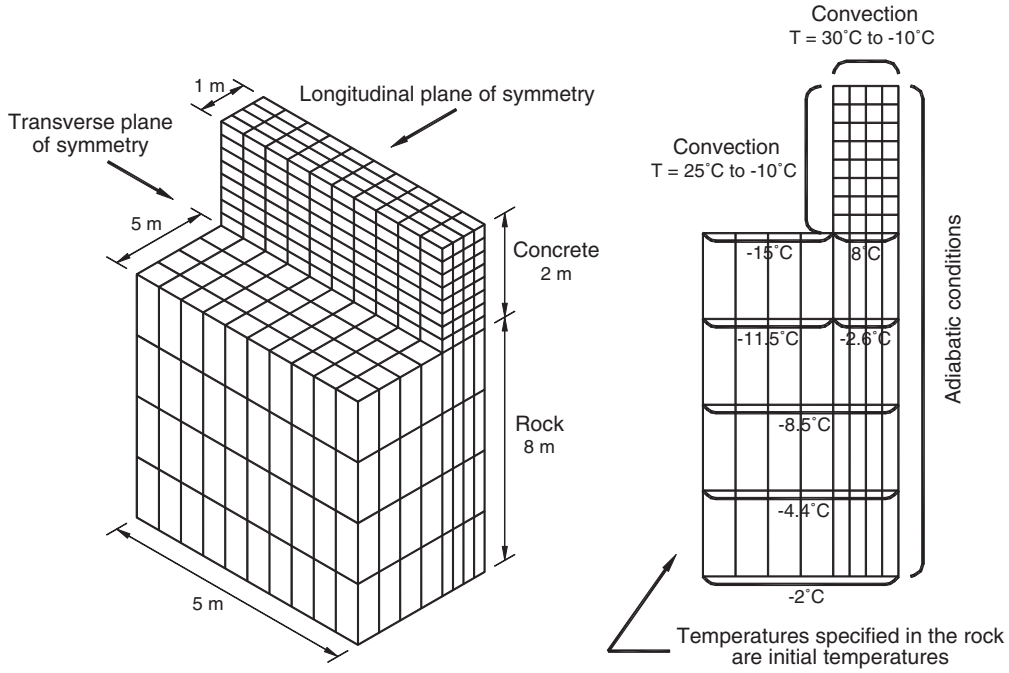

Fig. 3. 3D and 2D finite element meshes of specimen [7].

rock elements underneath the concrete elements. Three-dimensional discretization using 8-node elements is shown in Fig. 3. To reduce the computational process, the model took advantage of the two planes of symmetry. A total of 320 concrete elements and 320 rock elements were used. Since one of the purposes for the numerical analyses of this example structure is to verify whether the present numerical model can effectively simulate the thermal behavior of RC structures, the same finite element mesh used by Ayotte et al. [7] in their numerical simulation is adopted.

The model and the thermal boundary conditions are presented in Fig. 3. For the first 7 days, different convection coefficients were used on the various surfaces to simulate the presence of a formwork. After 7 days, coinciding with formwork removal, a uniform convection coefficient was used for all exposed surfaces. The variation of temperature at boundaries for the first 30 days following the casting of concrete is shown in Fig. 4. These variations correspond to measurements made in the shelter of the specimen.

Figs. 5 and 6 compare the analytical results with the measured temperatures in the specimen. Very satisfactory agreement between analysis and experiment is observed. The analytical results by Ayotte et al. [7] are also shown in these figures.

In Fig. 5, the variation of the calculated temperature at the center of the specimen (thermocouple 4 in Fig. 2) almost perfectly follows the measured variation as well as the simulated temperature variation by Ayotte et al. [7]. On the other hand, the temperature variation at a point near the top of the specimen (thermocouple 2 in Fig. 2) in the transverse plane still represents a small discrepancy between the simulated values and the measured ones at early age. As noted by Ayotte et al. [7], this difference appears to be caused by the variability of the exposure temperature inside the shelter, which could not be

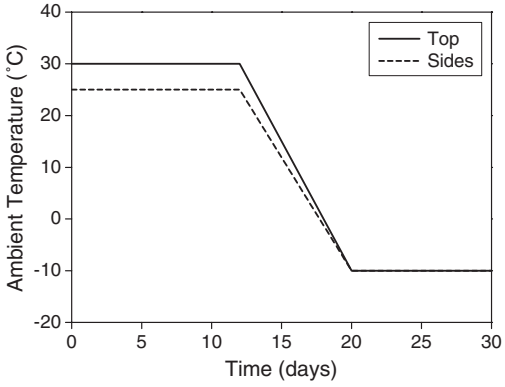

Fig. 4. Ambient temperature [7].

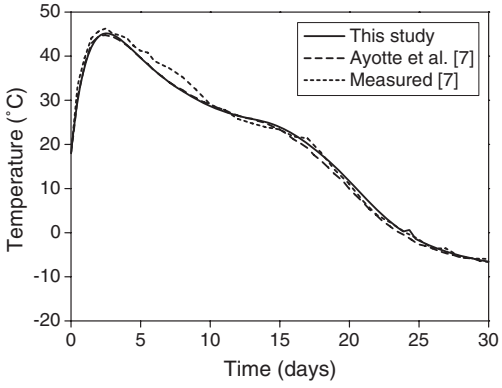

Fig. 5. Temperature comparison at the center of specimen (thermocouple 4 in Fig. 2).

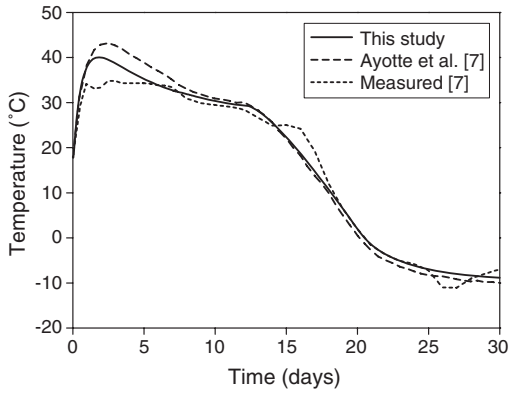

Fig. 6. Temperature comparison at the top of specimen (thermocouple 2 in Fig. 2).

maintained perfectly constant nor uniform. In advance, a comparison between the temperatures in the specimen (Figs. 5 and 6) and the temperatures on the boundaries (Fig. 4) shows that the temperature variations at both points in Figs. 5 and 6 are governed by the ambient temperature on the boundaries from the time at which the hydration heat has been dissipated by the heat convection (about 10 days after the placement of the concrete).

On the other hand, since the moisture diffusion takes place very slowly in a mass concrete such as this example structure, several years is required to reach a complete humidity balance between the structure and atmosphere. Therefore, the instrumentation for 30 days after the placement of the concrete appears to be insufficient to analyze the coupling effect between the heat transfer analysis and the moisture diffusion analysis, and the analysis considering the moisture diffusion effect in this example also represents very similar results with those presented in Figs. 5 and 6.

The second example is a rectangular concrete block tested by Kim and Lee [19], prepared to measure the internal relative humidity in concrete during drying. The specimen was submerged into water after demoulding at the age of 1 day and remained there until the test was started. After moist-curing, test specimens were exposed to a constant temperature of 20±1 °C and constant humidity of 50±2% relative humidity.

As shown in Fig. 7, the exposed area of the specimen is 10×10 cm, and the total depth of specimen is 20 cm. Five sides of the specimen were sealed with paraffin wax to ensure that only uniaxial moisture diffusion took place during the drying process. The plastic sleeves in which the relative humidity was measured were placed at distances of 3, 7, and 12 cm from the exposed surface. Material parameters and design variables used

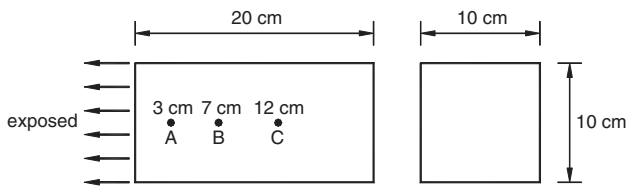

Fig. 7. Geometry and size of test specimen [19].

Table 2
Material properties used in the analysis

Water/cement ratio	0.4
Unit quantity of cement (kg/m^3)	423
28-day compressive strength (MPa)	53.0
Maximum moisture diffusion coefficient (m^2/h)	1.24×10^{-6}
Surface factor (m/h) [20 °C]	
3-day curing	1.71×10^{-5}
28-day curing	1.20×10^{-5}

in the analysis are given in Table 2, and more details related to the experimental study can be found elsewhere [19].

Figs. 8 and 9 show the distribution of relative humidity of the specimen subjected to drying when 3 and 28 days of moist-curing were employed, respectively. The analytical results are compared with the experimental measurements of Kim and Lee [19], and show good agreement. These figures also show that the relative humidity near the exposed surface decreased rapidly at the early stage of drying, but inside the concrete, the relative humidity varied very slowly. However, the decreasing rate of the relative humidity represents a uniform value regardless of the location with the lapse of time. Comparison of Figs. 8 and 9 also shows that the distribution of relative humidity in concrete is considerably influenced by initial moist-curing time. Increase of the curing time reduces the rate of decrease of the relative humidity: the rate of moisture diffusion is inversely proportional to the moist-curing time.

The final example is a full scale RC wall structure tested by Machida and Uehara [3], who instrumentally measured and theoretically calculated temperatures and stresses in several points of a thick wall of a nuclear power station during a period of 15 days after concreting. The wall is 1 m thick, 15 m long and has an average height of 4.2 m. It is cast on a large concrete basement, and dimensions and configuration of the example structure can be found in Fig. 10. This experiment is particularly valuable because the stresses have been measured directly. More details related to the experiment can be found in Ref. [3].

The measured temperatures and stresses at several points (see Fig. 11) were compared with theoretically calculated values obtained by Machida and Uehara [3]. Because of the insufficient precision in taking into account the air temperature and its daily variation, the solar radiation, and the influence of

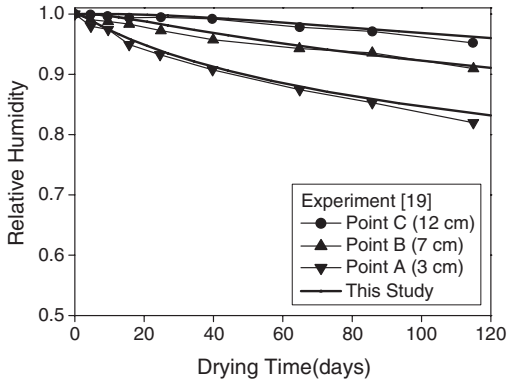

Fig. 8. Relative humidity values compared to experimental values (t_0=3 days).

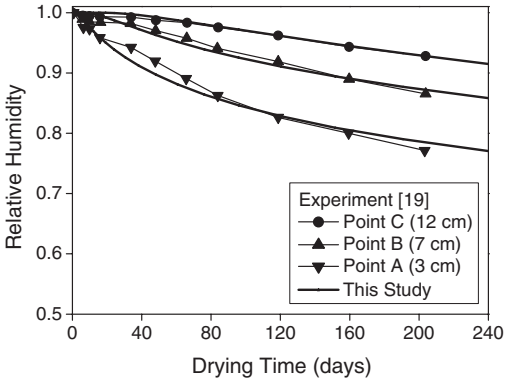

Fig. 9. Relative humidity values compared to experimental values (t_0=28 days).

the concrete temperature on cement hydration, however, some of the theoretical curves deviate significantly from the experimental values, with discrepancies as great as 5–10 °C for temperature and 0.5–1.0 MPa for stress (see Figs. 15 and 17). Clearly with such inaccuracy of the obtained theoretical stresses, any crack safety check will not be reliable. To describe the real phenomenon and to improve the numerical results, Santurjian and Kolarow [6] considered the daily varying air temperature curve according to the real data (see Fig. 12) in the numerical analyses and obtained improved numerical results. In addition, further differences and details for both analysis methods, such as the consideration of the directed insolation effect, adoption of an age function, and use of a creep compliance function for the creep formation, can be found in Ref. [6].

A three-dimensional solid element with 8 nodes is used to idealize the structure, and the finite element mesh model is shown in Fig. 13. The same mesh was also used in both of the previous numerical analyses. In this analysis, a half model of the total structure is used for reasons of symmetry along the wall thickness. The boundary conditions on the symmetry plane and on the outside faces of the basement and the subsoil are adiabatic. The temperature at the bottom of the subsoil is fixed at 17 °C. In particular, since both time-dependent temperature variations due to hydration heat and non-uniform moisture distribution during drying are taken into account, the influence of moisture variation on the hydration heat in the concrete is reflected, and more improved numerical results are expected. Unfortunately, however, material constants related to the moisture diffusion analysis were not defined anywhere because the experimental study and numerical analyses focused on the structural responses due to hydration heat, and hence appropriate values that could effectively describe the experimental conditions had to be assumed in this study. The material properties used in this analysis are given in Table 3.

Figs. 14 and 15 show the temperature variation at locations 33 and 36. Good coincidence between the measured and calculated temperature values at points 33 and 36 is evident, and the differences are less than 1.5 °C during the entire period of 14 days. The better results obtained by applying the present numerical model are basically due to the consideration of the daily air temperature variation in Fig. 12 and the directed solar radiation.

The temperature history calculated at location 36 (Fig. 15) represents a slightly larger difference from the experimental data. This is likely to be a result of the location of point 36, which is very close to the top surface of the wall and as such directly suffers from frequent temperature changes at boundaries, while the numerical model is limited in terms of effective consideration of the randomly fluctuating atmospheric temperature. On the other hand, after the hydration heat dissipates, the temperature distribution is predominantly governed by the atmospheric temperature. Specifically, the temperatures at locations near to the surface represent the same fluctuations with the atmospheric temperature.

The horizontal stress distributions at locations 40 and 42 are shown in Figs. 16 and 17, respectively. The results from the present model show an excellent agreement with the experimental results. On the other hand, the numerical results by Machida et al. represent relatively large discrepancies from the experimental data (once again because daily air temperature variation and the direct insolation effects were not considered).

The measurement stress histories in Figs. 16 and 17 also show that maximum compressive stress of −1.0 MPa occurred at the center point of the mid-length (see Figs. 11 and 16) 1 day after concrete placement, and the compressive stress became a tensile stress with the lapse of time. The upper point of the mid-length of the structure (see Figs. 11 and 17), however, has a tensile stress of 0.8 MPa after about 2 days, which becomes compressive again after 8 days with a value of −0.6 MPa. The proposed model also gives the maximum tensile and compressive stresses at the same time, although there is a slight difference in the maximum value for the tensile stress at the structure surface (see Fig. 17). That is, no clear peak in the tension region is obtained in the numerical analysis. Nevertheless, the overall stress history is well described by the proposed model.

In contrast to the proposed model, however, the numerical results of Machida et al. in Fig. 17 show the essential deviation of the calculated stresses from the experimental stress curves. This discrepancy is due to the absence of consideration of the material properties of concrete at an early age and due to an inaccurate prediction of temperature. The differences in the first 2 days are accumulated and enlarged with time. In particular, since the thermal and deformation processes are complex at an

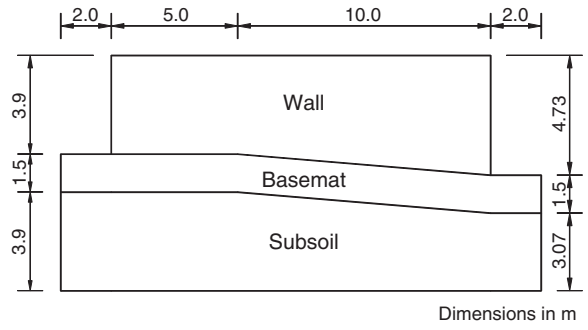

Fig. 10. Geometric configuration of wall [3].

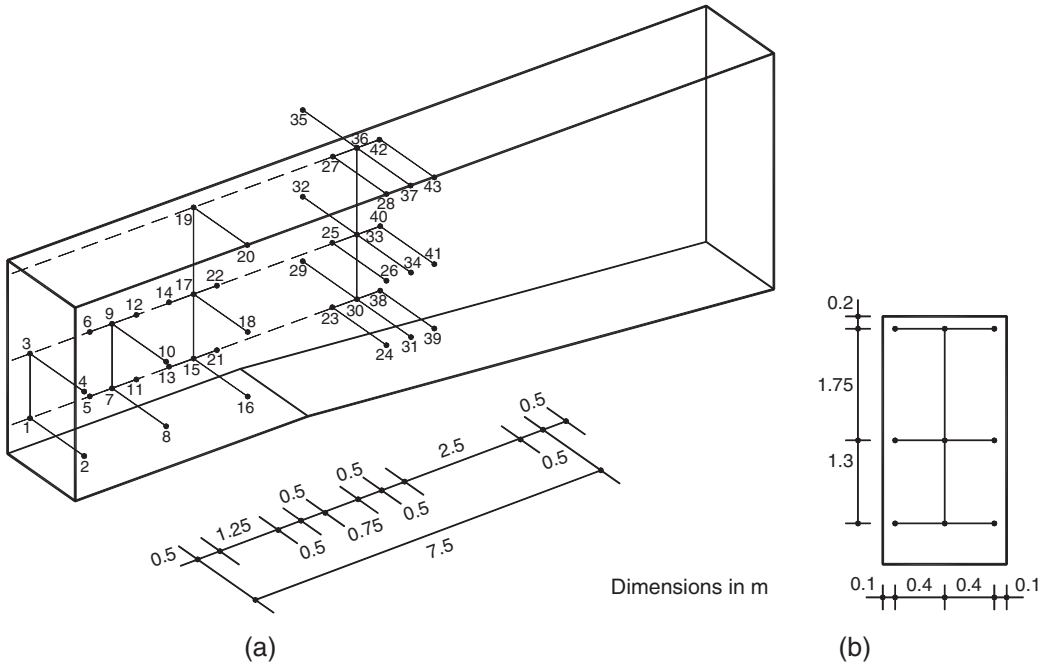

Fig. 11. Measurement locations [3]. (a) Instruments locations, (b) cross section.

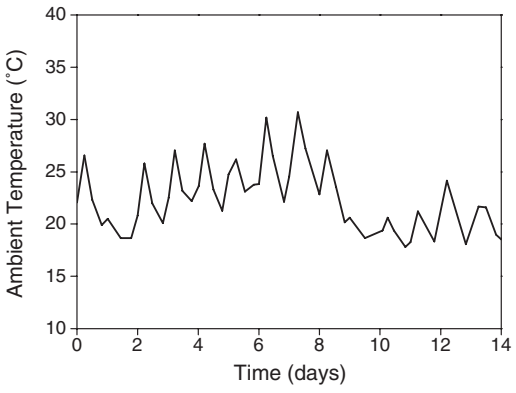

Fig. 12. Atmospheric temperature [3].

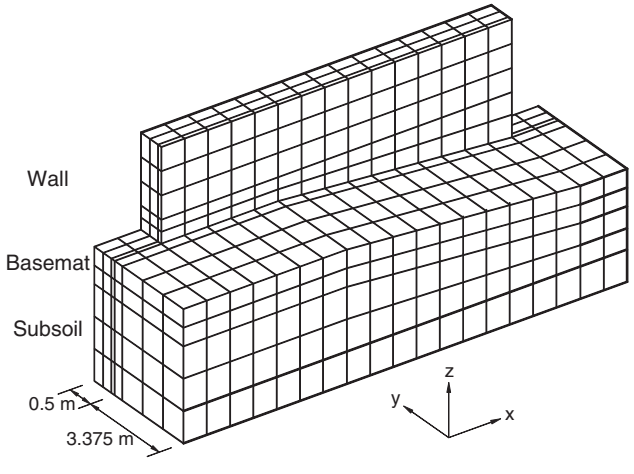

Fig. 13. Finite element idealization [3].

early time after placing the concrete, the accuracy of the numerical results depends on the consideration of material properties for the early age concrete. Obviously, the use of material properties for the fully hardened concrete is insufficient to trace the non-structural cracking behavior of concrete, and the excellent agreement with experimental results obtained using the proposed model reflects the consideration of the material properties for the early age concrete.

6. Conclusions

This paper proposes a three-dimensional finite element model for the analysis of non-structural cracking in RC walls.

Table 3
Material properties used in the analysis

Material property	Concrete	Basement	Subsoil
Water/cement ratio	0.598	0.598	–
Unit quantity of cement (kg/m^3)	266	266	–
28-day compressive strength (MPa)	26.5	26.5	–
Density (kg/m^3)	2320	2320	1700
Specific heat (J/kg °C)	984	984	2052
Thermal conductivity (W/m °C) [20 °C, RH 100%]	2.00	2.00	1.23
Convection coefficient (W/m^2 °C)	10.5	–	–
Maximum adiabatic temperature rise (°C)	37.0	–	–
Reaction rate (day^{-1})	2.0	–	–
Maximum moisture diffusion coefficient (m^2/h)	1.55×10^{-6}	1.55×10^{-6}	–
Surface factor (m/h) [20 °C]	1.66×10^{-5}	–	–
Coefficient of expansion (°C^{-1})	1×10^{-5}	1×10^{-5}	1×10^{-5}
Elastic modulus (GPa) [20 °C]	27.0 (28-day)	27.0	0.127
Poisson's ratio	0.167	0.167	0.4

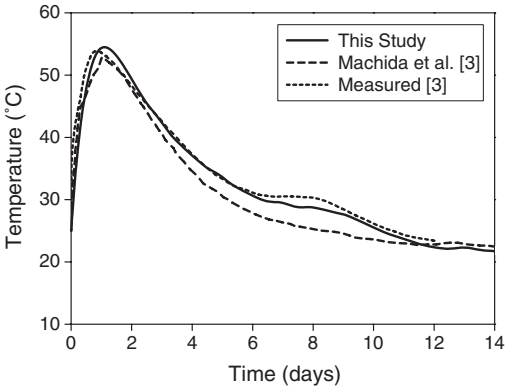

Fig. 14. Temperature history at the center of wall (location 33).

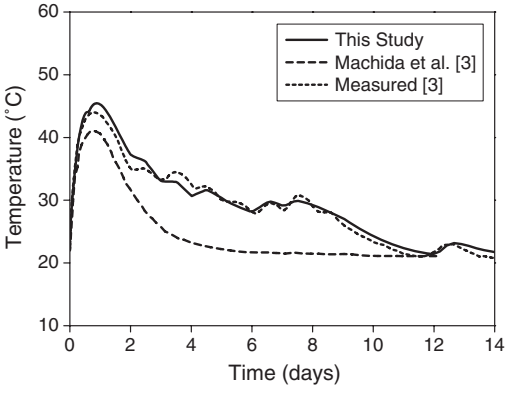

Fig. 15. Temperature history at the top of wall (location 36).

Unlike the other numerical approaches, both heat transfer analysis to trace the time-dependent temperature variations due to hydration heat and moisture diffusion analysis to consider the non-uniform moisture distribution across the depth are conducted to evaluate the possibility of cracking. Specifically, the material properties of concrete at early age, directly determined from numerous experimental studies [4,9,20], are taken into consideration, and the dependent long-term deformations of concrete (creep and shrinkage) are also considered in this paper. To verify the proposed numerical model, comparisons between analytical results and experimental data are

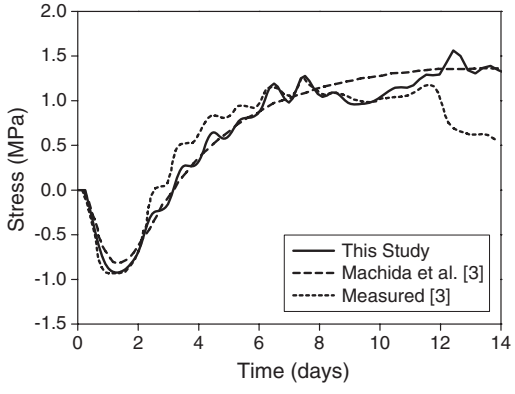

Fig. 16. Stress history at the center of wall (location 40).

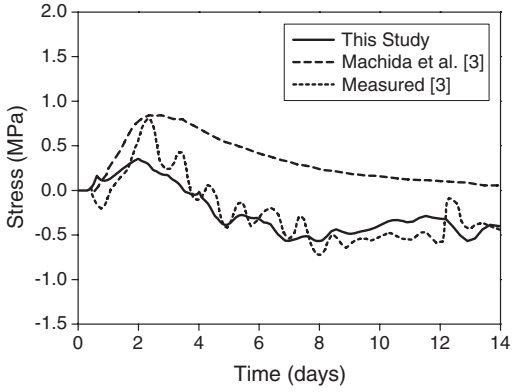

Fig. 17. Stress history at the top of wall (location 42).

performed, and excellent agreements with experimental results are obtained for all example structures. Accordingly, the proposed model can effectively be used to quantitatively estimate the occurrence of non-structural cracking in RC walls.

Acknowledgements

The authors would like to thank the Infrastructures Assessment Research Center (ISARC) funded by Korea Ministry of Construction and Transportation (MOCT) for financial support.

References

[1] A.M. Neville, Properties of Concrete, John Wiley & Sons, New York, 1997.
[2] Z.P. Bazant, W. Thonguthai, Pore pressure and drying of concrete at high temperature, J. Eng. Mech.-ASCE 104 (EM5) (1978) 1059–1079.
[3] N. Machida, K. Uehara, Nonlinear thermal stress analysis of a massive concrete structure, Comput. Struct. 26 (1/2) (1987) 287–296.
[4] H. Mihashi, T. Numao, Influence of curing condition on a diffusion process of concrete at elevated temperatures, Proc. Jpn. Concr. Inst. 11 (1) (1989) 229–234.
[5] J.K. Kim, S.H. Eo, C.S. Lee, Y.Y. Kim, Development of Cracking Analysis Program for Differential Drying Shrinkage of Concrete Structure, Res. Rep. 94-020, Electrical Engineering and Science Research Institute, Korea, 1995.
[6] O. Santurjian, L. Kolarow, A spatial FEM model of thermal stress state of concrete blocks with creep consideration, Comput. Struct. 58 (3) (1996) 563–574.
[7] É. Ayotte, B. Massicotte, J. Houde, V. Gocevski, Modeling the thermal stresses at early ages in concrete monolith, ACI Mater. J. 94 (6) (1997) 577–587.
[8] A.A. Khan, W.D. Cook, D. Mitchell, Thermal properties and transient thermal analysis of structural members during hydration, ACI Mater. J. 95 (3) (1998) 293–303.
[9] Y.C. Song, M.S. Cho, W.S. Jeoung, G.S. Pang, S.K. Woo, Reduction of Hydration Heat in Concrete Structures, Res. Rep. TR.96NJ24.J1998.62, Korea Electric Power Research Institute, Korea, 1998.
[10] D. Cusson, W.L. Repette, Early-age cracking in reconstructed concrete bridge barrier walls, ACI Mater. J. 97 (4) (2000) 438–446.
[11] 42-CEA Committee, Properties of set concrete at early ages: state of the art report, Mater. Struct. 14 (84) (1981) 399–450.
[12] ACI Committee 207, Mass Concrete (ACI 207.1R-96), ACI Manual of Concrete Practice, American Concrete Institute, Detroit, 1996.
[13] Z.P. Bazant, L.J. Najjar, Nonlinear water diffusion in nonsaturated concrete, Mater. Struct. 5 (25) (1972) 3–20.

[14] T.C. Powers, Mechanisms of shrinkage and reversible creep of hardened cement paste, Proceeding of International Conference on the Structure of Concrete, Cement and Concrete Association, London, 1965, pp. 319–344.
[15] Sikoku Electric Power Corporation, A Study on the Preventive Measure of Early-Age Cracking in a Mass Concrete, Res. Rep., Japan, 1964.
[16] K. Sakata, A study on moisture diffusion in drying and drying shrinkage of concrete, Cem. Concr. Res. 13 (2) (1983) 216–224.
[17] Japan Concrete Institute, Thermal Stress in Mass Concrete, JCI State-of-the-art Report, Japan Concrete Institute, Japan, 1985.
[18] Comite Euro-International du Beton, CEB-FIP Model Code 1990: Design Code, Thomas Telford, London, 1993.
[19] J.K. Kim, C.S. Lee, Moisture diffusion of concrete considering self-desiccation at early ages, Cem. Concr. Res. 29 (12) (1999) 1921–1927.
[20] J.K. Kim, S.H. Han, S.K. Park, Effect of temperature and aging on the mechanical properties of concrete: Part II. Prediction model, Cem. Concr. Res. 32 (7) (2002) 1095–1100.
[21] H.G. Kwak, F.C. Filippou, A new reinforcing steel model with bond-slip, Struct. Eng. Mech. 3 (4) (1995) 299–312.
[22] R.D. Cook, D.S. Malkus, M.E. Plesha, Concepts and Applications of Finite Element Analysis, John Wiley & Sons, New York, 1989.
[23] Y.J. Kang, Nonlinear Geometric, Material and Time-Dependent Analysis of Reinforced and Prestressed Concrete Frame, Rep. No. UC-SEEM 77-1, Univ. of California, Berkeley, 1977.